Supporting Information

Organic-inorganic hybrid p-n junction composite for high-performance carbon monoxide gas sensing and mechanistic understanding using *in situ* Raman spectroscopy

Karthigeyan P. S.[a,b], Sasi Karan R. R.[a,b], Hariramakrishnan S.[a,b], Adityan S.[a,b], Tamilarasan P.[a,b,*]

[a]Electrodics and Electrocatalysis Division (EEC), CSIR-Central Electrochemical Research Institute (CECRI), Karaikudi 630003. Tamil Nadu. India.

[b]Academy of Scientific and Innovative Research (AcSIR), Ghaziabad 201 002, India.

*Corresponding author email: tamilan.cecri@csir.res.in

Table of Contents

ESI 1. Materials and Instrumentation

1.1 Materials

Tungsten disulfide (WS_2) and Dimethylformamide (DMF) were purchased from Sigma Aldrich. Poly(3,4-ethylenedioxytiophene)-polystyrenesulfonate (PEDOT:PSS) (1.25 wt%) was obtained from Polysciences. Glass slides (26x76 mm, thickness 1-1.2 mm) were procured from Lab Tech Micro Pvt. Limited. These materials were used without further purification. Unless otherwise mentioned, deionised water (resistivity: 18.2 MΩ-cm) was used for all experiments.

1.2 Apparatus and equipment

The bulk WS_2 was mechanically exfoliated using a Sonics VX-500 probe sonicator (~20 kHz frequency) with 500 W maximum power. The Raman spectra of the samples were acquired using a Renishaw Invia Spectrometer with a 785 nm laser. The crystallographic structure was confirmed through Grazing Incidence X-ray Diffraction (GIXRD) using a Rigaku SmartLab guidance (the power of 200mA, 45 kV) X-ray diffractometer for thin-film analysis obtained in the 2θ range from 5° to 90° and at 3° per min, using copper Kα radiation (λ= 1.54 Å). X-ray Photoelectron Spectroscopy (XPS) was deployed to analyse chemical composition and oxidation states using a Thermo Scientific ESCALAB 250 Xi spectrometer. High-Resolution Transmission Electron Microscopy (HRTEM) using FEI TalosF200S was used for surface morphology imaging, while Energy Dispersive X-ray Analysis (EDX) was used for elemental composition analysis, utilising the Talos EDX FEI, Netherlands (model: Super S) system. Carl Zeiss SUPRA 55VP was used for the FESEM (Field Emission Scanning Electron Microscope) images. The T-shaped Au/Ti (100 nm/5 nm) electrodes with a 30 μm channel width were deposited through a stencil using Hydro Pneo Vac Technologies (India) electron beam evaporation system inside an ISO 7 cleanroom. The gas sensing analyses were done using a controlled gas sensing chamber (Hydro Pneo Vac Technologies, India) where the ohmic electrical contacts were established by precision micropositioners with gold-coated tungsten probes (tip diameter: 20 μm). The gas supply was controlled using Alicat multi-gas mass flow controllers. The change in current (and thus resistance) under applied bias was monitored using a Keithley 2612B sourcemeter.

ESI 2. Conductivity comparison via I-V characterization

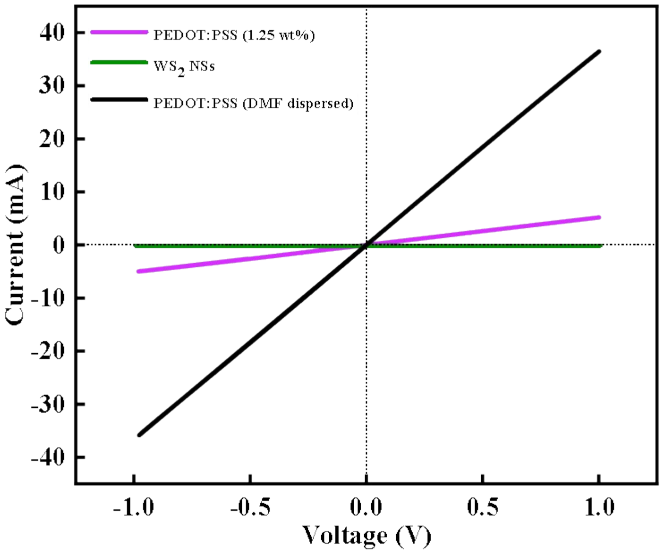

Figure S1. Comparative I-V characteristics of devices with WS_2 NSs and PEDOT:PSS channel.

In **Figure S1** conductivity comparison among WS_2 NSs, bare PEDOT:PSS (1.25 wt% in aqueous medium), and DMF-dispersed PEDOT:PSS reveals a clear trend. WS_2 NSs, being intrinsic semiconductors, exhibit relatively low conductivity. In contrast, aqueous-dispersed PEDOT:PSS demonstrated moderate conductivity due to its polymeric nature. However, when PEDOT:PSS is dispersed in a polar organic solvent DMF, a significant enhancement in conductivity is observed. This improvement is attributed to the disruption of Coulomb interactions between $PEDOT^+$ and PSS^- chains, leading to a more conductive and better-organised $PEDOT^+$ polymer network. As reported earlier, the addition of polar organic solvents such as DMF improves the film uniformity and electrical conductivity of PEDOT:PSS by weakening Coulomb interactions between $PEDOT^+$ and PSS^-, promoting better phase separation and charge transport. Moreover, the structural transition from the benzoid to the more conductive quinoid form in PEDOT enhances π-conjugation and chain linearity, resulting in an enhancement of electrical properties.

ESI 3. Raman spectrum of WNPP composite

The exfoliated WS_2 NSs perfectly embedded into the polymer matrix are confirmed by using Raman spectroscopy to take spectra from the different regions. For the PEDOT:PSS Oxyethylene ring deformation occurs at 439 cm^{-1}, 525 cm^{-1}, and 947 cm^{-1}, indicating structural stability. The 578 cm^{-1} mode corresponds to C$_\alpha$–C$_\alpha$–C$_\beta$ bending vibrations coupled with ethylenedioxy ring contributions, while the 701 cm^{-1} band is attributed to symmetric C–C–C bending influenced by ethylenedioxy ring vibrations. The 991 cm^{-1} mode represents ethylenedioxy ring bending along with C$_\alpha$–C$_\alpha$–C$_\beta$ deformation, and the 1099 cm^{-1} peak corresponds to in-plane C–H bending. Further, the 1149 cm^{-1} band is associated with C–O–C deformation, while 1220 cm^{-1} corresponds to inter-ring C–C stretching combined with C–H bending. The 1258 cm^{-1} peak signifies C$_\alpha$–C$_\alpha$ stretching, whereas 1371 cm^{-1} represents a combination of C$_\beta$–C$_\beta$ and C$_\alpha$–C$_\alpha$ stretching vibrations. The symmetric stretching of C$_\alpha$–C$_\beta$ bonds occurs at 1424 cm^{-1} in the reduced state, while asymmetric stretching is observed at 1529 cm^{-1} in the oxidised state and at 1552 cm^{-1} in the reduced state [1, 2].

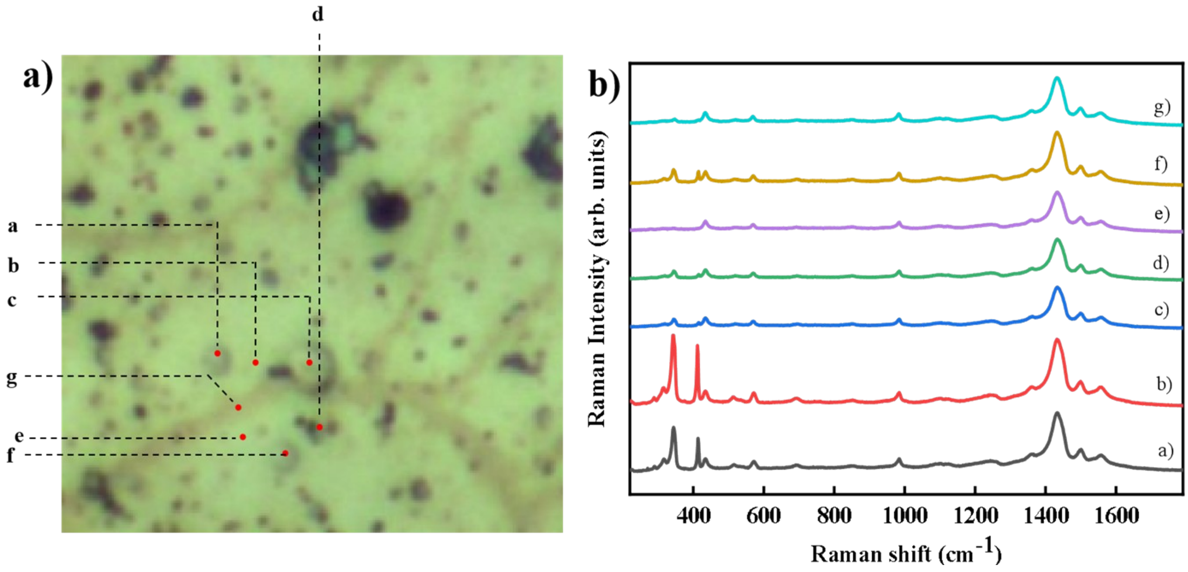

Figure S2. Raman spectrum of WNPP. **(a)** Optical image of the sample with marked spots and **(b)** Raman spectra at the marked spots.

ESI 4. Calculation of d-spacing from XRD peaks

Using Bragg's law:

$$d = \frac{\lambda}{2\,Sin\theta}$$

Peak position, 2θ =14.2°. Thus, θ = 7.1°

$$d = \frac{1.5406}{2\;X\;0.2472} = \frac{1.5406}{0.2472} = 0.623 \text{ nm or } 6.23\ \text{Å}$$

The XRD peak at $2\theta = 14.2°$ corresponds to the (002) crystal plane of 2H-WS_2. The calculated interlayer d-spacing from this peak is approximately 0.623 nm, which aligns well with typical values for the spacing between WS_2 layers in the hexagonal structure. This confirms the layered nature of the exfoliated WS_2 NS [3].

Compared to bulk, exfoliated few-layer or monolayer WS_2 NSs offer more active sites with higher activity due to a higher surface-to-volume ratio. The transition from an indirect-to-direct band gap enhances the density of states near the Fermi level, improving charge transfer and boosting sensing sensitivity. Additionally, the presence of high-energy surface atoms enhances chemical reactivity and gas adsorption efficiency [4, 5].

ESI 5. HRTEM of exfoliated WS_2 NSs and composite

From the SAED analysis, a value of 7.159 nm^{-1} was obtained, which corresponds to the reciprocal of twice the radius (1/2r). To calculate the in-plane lattice spacing, this value was first divided by 2, yielding 3.5795 nm^{-1}, which represents 1/d. Taking the inverse of this value, the lattice spacing was calculated as $d=1/3.5795 = 0.2794$ nm. In **Figure S3 (a)**, clear lattice fringes from the exfoliated WS_2 NSs are observed, exhibiting an in-plane lattice distance of 0.276 nm. In **Figure S3 (b)**, the exfoliated nanosheets embedded within the polymer matrix are clearly visible, confirming successful incorporation into the composite.

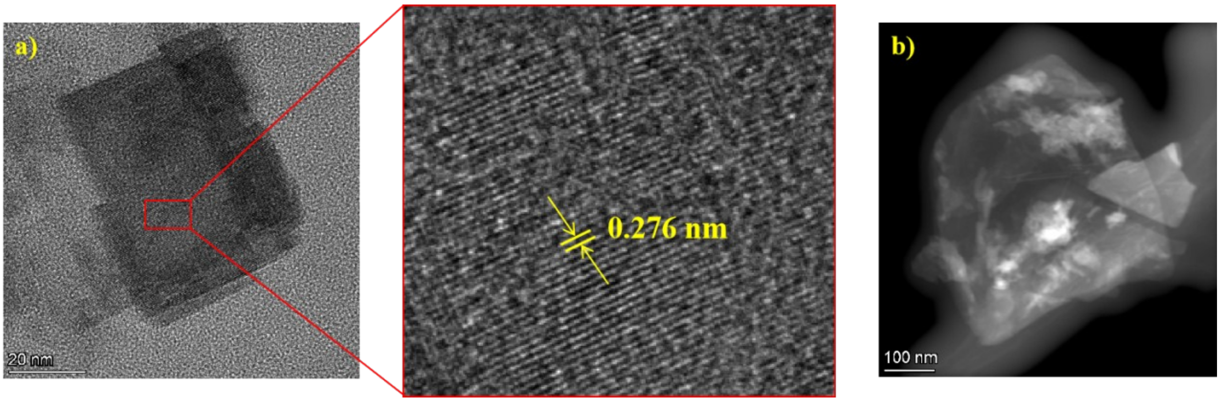

Figure S3. (a) HRTEM image of WS_2 NSs and **(b)** HAAEDF image of WNPP.

The energy dispersive X-ray spectrum for the WNP in **Figure S4** shows a high carbon content (72.2%), reflecting the carbon-rich PEDOT:PSS polymer uniformly distributed in the composite, Tungsten (7.3%), sulphur (18.7%), and oxygen (1.2%) due to PEDOT:PSS and also some from WO_x.

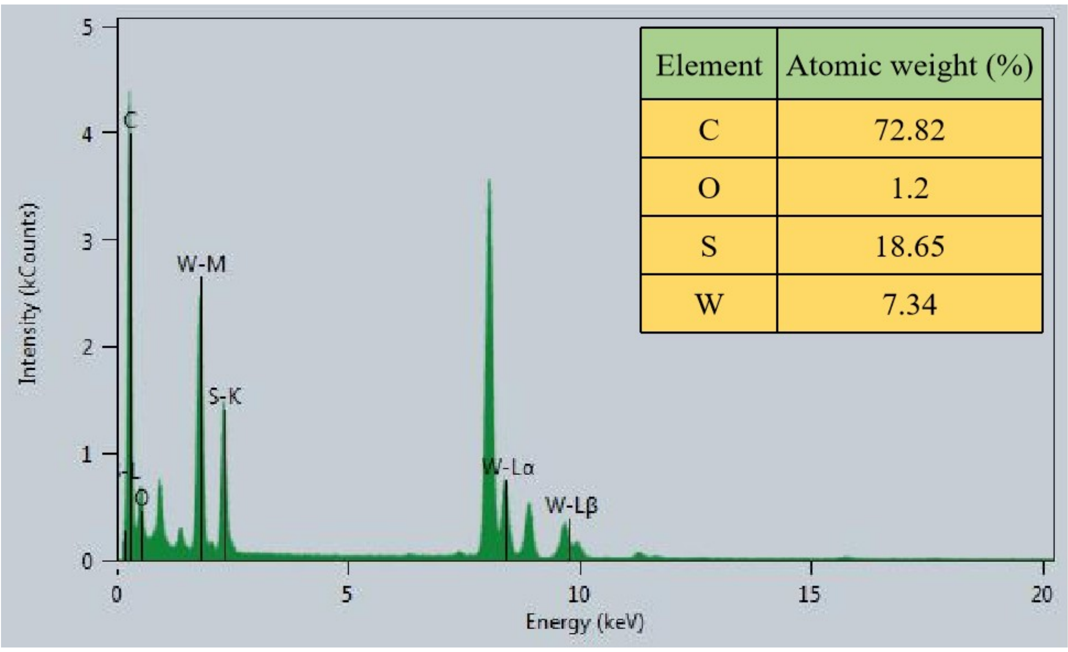

Figure S4. WNPP EDS spectrum.

ESI 6. Comparative surface elemental analysis of WS_2 NSs and WNPP

The elemental composition of WS_2 NSs and WNPP was compared to assess changes in surface chemistry and purity after processing. In pristine exfoliated WS_2 NSs, Tungsten (W 4d) accounted for 14.08 At% and sulfur (S 2p) for 1.58 At%, respectively. Notably, the sample showed a dominant oxygen (O 1s) content of 83.29 At%, likely due to heavy surface oxidation or exposure to ambient air. The carbon (C 1s) content was minimal at 1.04 At%, indicating relatively low organic contamination in the pristine sample.

Table S1. WNPP Atomic percent from XPS.

Element	WS_2 NSs Atomic %	(WNPP)Atomic %
W 4d	14.08	8.23
S 2p	1.58	11.58
C 1s	1.04	48.77
O 1s	83.29	31.41

In contrast, the WNPP sample exhibited a lower W 4d atomic percentage (8.23 At%) but a substantial increase in S 2p (11.58 At%), indicating improved sulphur retention. The significant reduction in oxygen content (48.77 At%) compared to the pristine sample, along with a marked increase in carbon (31.41 At%), suggests surface modification through organic functionalization of a carbon-rich PEDOT:PSS matrix.

ESI 7. Effect of WNPP composite ratio on CO sensing

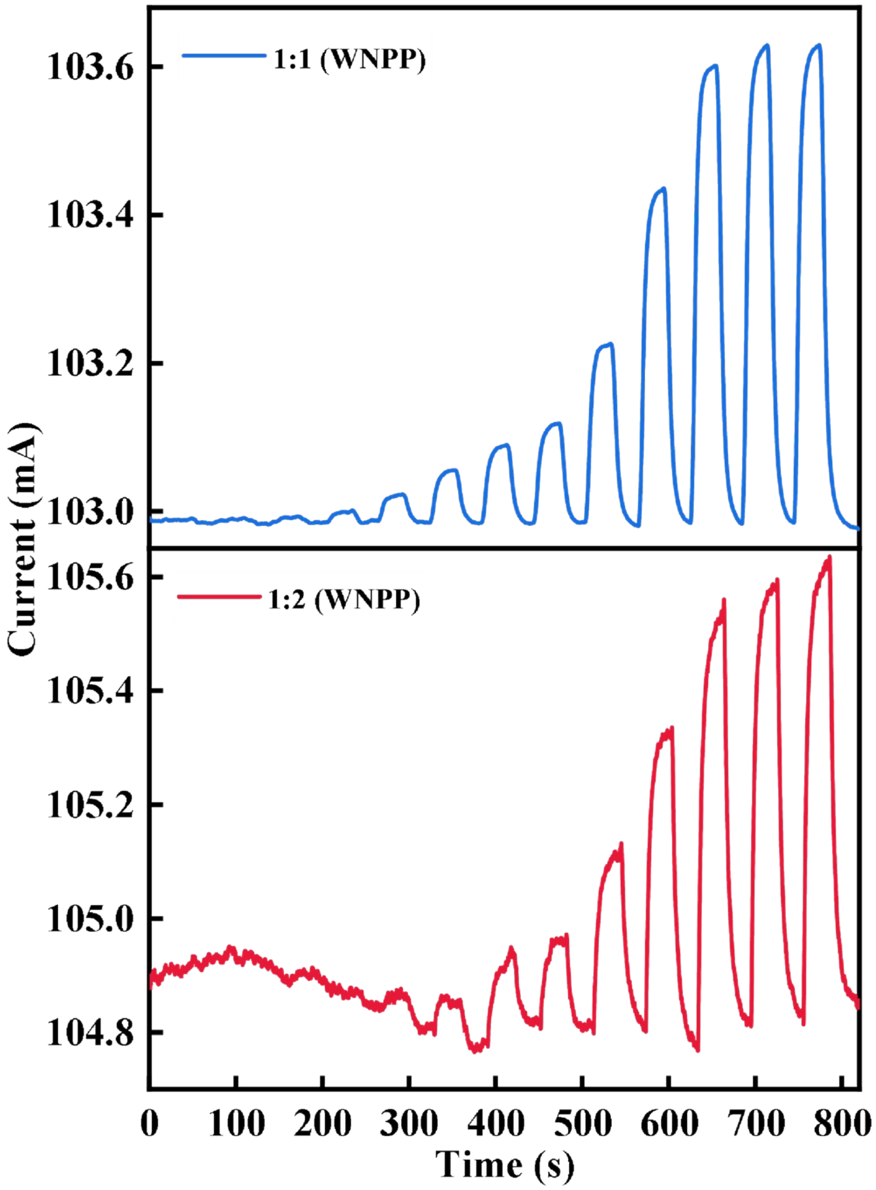

Figure S5. 1:1 (w/w) and 1:2 (w/w) of WNPP composites CO response (1 to 1000 ppm)

When comparing the 1:2 and 1:1 (w/w) composite, 1:1 exhibited the best performance, showing enhanced baseline stability and increased sensitivity, including detection of lower CO concentrations (Figure S5). This improvement arises from the optimal interaction between n-type WS_2 and p-type PEDOT:PSS, forming effective p-n heterojunctions that facilitate charge separation and boost charge transport during gas exposure.

ESI 8. Carrier gas influence on 25 ppm CO detection

To confirm the sensing mechanism, CO responses were measured using air and nitrogen (N_2) as carrier gases (**Figure S7**). Under N_2, the device showed noisier signals and lower sensitivity due to the lack of oxygen needed for forming adsorbed oxygen species. However, CO still interacted directly with WS_2 active sites. Overall, sensing was less effective in N_2, highlighting oxygen's key role in enhancing performance.

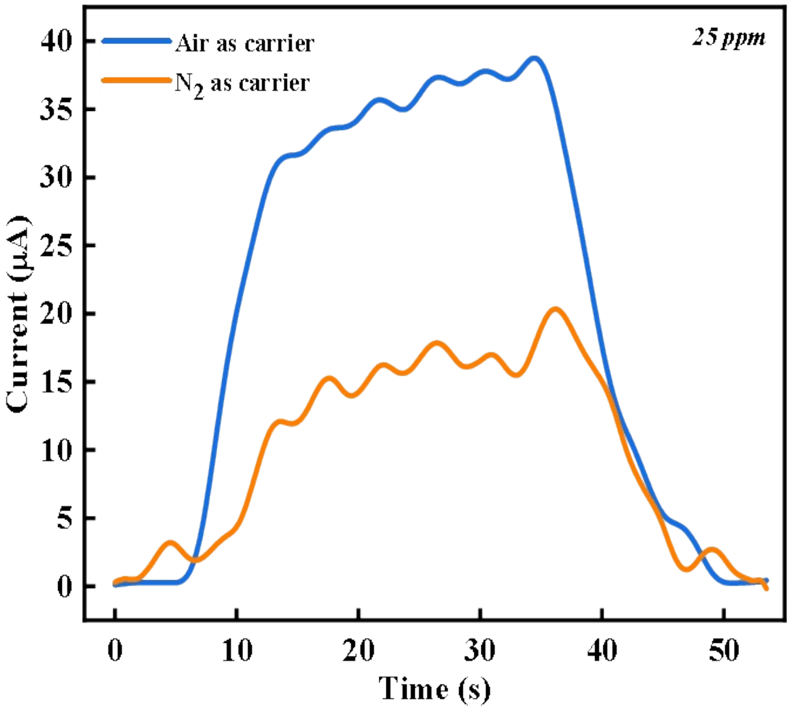

Figure S7. CO gas response at 25 ppm using different carrier gases.

ESI 9. Earlier reports

Table S2. WS_2-based CO gas sensing performance of organic component-based sensors: Previous reports versus our work.

Sensing material	Operating temperature (°C)	Detection range (ppm)	Response		Res/Rec Time (s)	Ref
			Value	Concentration used		
PPy-GO	RT	50-300	45%[a]	-	89/95	[6]
Au-decorated WS_2	25	0.1-50	1.48[b]	50 ppm	175/25	[7]
Au-decorated Sb-WS_2 composite	20	-	3.9[b]	51 ppm	23/410	[8]
Au-decorated 10 wt% SnO_2-WS_2 composite	20	-	105[a]	52 ppm	355/275	[9]
PEDOT:PSS/Fe (Salem)	RT	10 - 100	1.5[b]	-	38	[10]
PEDOT:PSS/PPA	RT	50 - 300	18.5 %[a]	100	58/61	[11]
SnO_2/PPy/GO	RT	5 - 50	252[c]	10	85/65	[12]
ZnO nanoroad	50	-	8 %[a]	15	10/12	[13]
PANI/Ti_3AlC_2/CeO_2	RT	100 - 500	0.14 %[a]	500	-	[14]
WS_2 NSs@PEDOT:PSS	RT	1 - 600	20.4[d]	25	5/8.5	This work

[a] ($\Delta R/R_a$), [b] R_a/R_g, and [c] ($\Delta I/I_a$). ΔR is the difference in resistance values of the sensor between the target gas (R_g) and air (R_a).

ESI. Reference

1. S. Sakamoto, M. Okumura, Z. Zhao and Y. Furukawa, *Chemical Physics Letters*, 2005, **412**, 395-398.
2. G. L. S. Garreau, J. P. Buisson, G. Froyer, and S. Lefrant, *Macromolecules*, **Vol. 32, No. 20, 1999**.
3. H. Long, L. Tao, C. Y. Tang, B. Zhou, Y. Zhao, L. Zeng, S. F. Yu, S. P. Lau, Y. Chai and Y. H. Tsang, *Nanoscale*, 2015, **7**, 17771-17777.
4. F. Song and X. Hu, *Nat Commun*, 2014, **5**, 4477.
5. M. Saliba, J. P. Atanas, T. M. Howayek and R. Habchi, *Nanoscale Adv*, 2023, **5**, 6787-6803.
6. M. A. Farea, H. Y. Mohammed, P. W. sayyad, N. N. Ingle, T. Al-Gahouari, M. M. Mahadik, G. A. Bodkhe, S. M. Shirsat and M. D. Shirsat, *Applied Physics A*, 2021, **127**.
7. J.-H. Kim, A. Mirzaei, H. W. Kim and S. S. Kim, *Sensors and Actuators B: Chemical*, 2019, **296**.
8. J. H. Kim, I. Sakaguchi, S. Hishita, T. Ohsawa, T. T. Suzuki and N. Saito, *Sensor Actuat B-Chem*, 2023, **382**.
9. J.-H. Kim, I. Sakaguchi, S. Hishita, T. T. Suzuki and N. Saito, *Chemosensors*, 2022, **10**.
10. F. Arabloo, S. Javadpour, R. Memarzadeh, F. Panahi, M. D. Emami and M. H. Shariat, *Synthetic Metals*, 2015, **209**, 192-199.

11. M. O. Farea, H. A. Alhadlaq, Z. M. Alaizeri, A. A. A. Ahmed, M. O. Sallam and M. Ahamed, *ACS Omega*, 2022, **7**, 22492-22499.

12. M. A. Farea, N. Yusof, H. Y. Mohammed, M. N. Murshed, M. E. El Sayed and D. Abdelhameed, *Materials Science in Semiconductor Processing*, 2025, **188**.

13. S. Dhall, K. Sood, J. Prakash and B. R. Mehta, *Physica Scripta*, 2024, **99**.

14. Z. Yang, X. Hu, M. Wu, J. Mao, N. Yang, X. Wang and Q. Zhang, *Journal of Molecular Structure*, 2025, **1322**.